ZEUS-prel-05-027

Submitted to the
XXXIII International Conference on High Energy Physics
July 26 - August 2, 2006, Moscow, Russia

Abstract: 14 **Session: QCD hard interactions**

Subjet distributions in inclusive-jet production in deep inelastic scattering at HERA

ZEUS Collaboration

Abstract

Subjet distributions have been measured in neutral current deep inelastic ep scattering with the ZEUS detector at HERA using an integrated luminosity of 81.7 pb^{-1}. Jets were identified using the k_T cluster algorithm in the longitudinally invariant inclusive mode in the laboratory frame. Subjets, or jet-like substructures within jets, were then defined as the number of clusters resolved in a jet by reapplying the jet algorithm at a smaller resolution scale $y_{\rm cut}$. Measurements of subjet distributions are presented as functions of the ratio between the subjet transverse energy and that of the jet, the difference between the subjet pseudorapidity (azimuth) and that of the jet, and $\alpha^{\rm sbj}$, the angle, as viewed from the jet centre, between the highest transverse energy subjet and the beam line in the pseudorapidity-azimuth plane. The measured normalised cross sections were used to study the pattern of parton radiation by comparing them with leading-logarithm parton-shower Monte Carlo models and perturbative QCD calculations.

1 Introduction

Jet production in ep collisions provides a fruitful testing ground of perturbative QCD (pQCD). Measurements of differential cross sections for jet production [1–3] have allowed detailed studies of parton dynamics, tests of the proton and photon parton distribution functions (PDFs) as well as precise determinations of the strong coupling constant, α_s. Another aspect of QCD, namely gluon emission from a primary quark, has been investigated by means of the internal structure of jets; this study gives insight into the transition between a parton produced in a hard process and the experimentally observable jet of hadrons. Previous analysis in neutral current (NC) deep inelastic scattering (DIS) were done by measuring the mean subjet multiplicity [4] and the mean integrated jet shape [5] and values of $\alpha_s(M_Z)$ were also extracted. In the present study, the pattern of QCD radiation is investigated by means of the subjet topology, yielding a very stringent test of pQCD calculations.

At sufficiently high jet transverse energy, $E_T^{\rm jet}$, where fragmentation effects become negligible, the jet structure can be calculated perturbatively. The lowest non-trivial-order contribution to the jet substructure is given by $\mathcal{O}(\alpha_s)$ pQCD calculations for NC DIS in the laboratory frame. Next-to-leading-order (NLO) calculations of jet substructure are available in this frame since it is possible to have three partons inside one jet.

In this paper, measurements of normalised differential subjet cross sections are presented. The measurements have been done as functions of the ratio between the subjet transverse energy and that of the jet, $E_T^{\rm sbj}/E_T^{\rm jet}$, the difference between the subjet pseudorapidity (azimuth) and that of the jet, $\eta^{\rm sbj} - \eta^{\rm jet}$ ($|\phi^{\rm sbj} - \phi^{\rm jet}|$), and $\alpha^{\rm sbj}$, the angle, as viewed from the jet centre, between the highest transverse energy subjet and the beam line in the pseudorapidity-azimuth plane. The measurements have been compared with the predictions of leading-logarithm parton-shower Monte Carlo (MC) models and pQCD calculations.

2 Subjet definition

Studies of QCD using jet production in NC DIS at HERA are usually performed in the Breit frame. The analysis of subjets presented here was performed in the laboratory frame, since calculations of this observable in the Breit frame can, at present, only be performed to $\mathcal{O}(\alpha_s)$. Calculations of the subjet distributions can be performed up to $\mathcal{O}(\alpha_s^2)$ in the laboratory frame since a jet can consist of up to three partons. Furthermore, the analysis was performed in the kinematic region defined by $Q^2 > 125$ GeV^2 since, at lower values of Q^2, the sample of events with at least one jet of $E_T^{\rm jet} > 14$ GeV is dominated by dijet events.

The k_T cluster algorithm [6] was used in the longitudinally invariant inclusive mode [7] to define jets in the hadronic final state. Subjets were resolved within a jet by considering all particles associated with the jet and repeating the application of the k_T cluster algorithm until, for every pair of particles i and j the quantity $d_{ij} = \min(E_{T,i}, E_{T,j})^2 \cdot ((\eta_i - \eta_j)^2 + (\phi_i - \phi_j)^2)$, where $E_{T,i}$, η_i and ϕ_i are the transverse energy, pseudorapidity and azimuth of particle i, respectively, was greater than $d_{\rm cut} = y_{\rm cut} \cdot (E_T^{\rm jet})^2$. All remaining clusters were called subjets. The subjet multiplicity depends upon the value chosen for the resolution parameter $y_{\rm cut}$.

3 Experimental set-up

A detailed description of the ZEUS detector can be found elsewhere [8,9]. A brief outline of the components that are most relevant for this analysis is given below.

Charged particles are tracked in the central tracking detector (CTD) [10], which operates in a magnetic field of 1.43 T provided by a thin superconducting solenoid. The CTD consists of 72 cylindrical drift-chamber layers, organized in nine superlayers covering the polar-angle[1] region $15^\circ < \theta < 164^\circ$. The transverse-momentum resolution for full-length tracks can be parameterised as $\sigma(p_T)/p_T = 0.0058 p_T \oplus 0.0065 \oplus 0.0014/p_T$, with p_T in GeV. The tracking system was used to measure the interaction vertex with a typical resolution along (transverse to) the beam direction of 0.4 (0.1) cm and to cross-check the energy scale of the calorimeter.

The high-resolution uranium–scintillator calorimeter (CAL) [11] covers 99.7% of the total solid angle and consists of three parts: the forward (FCAL), the barrel (BCAL) and the rear (RCAL) calorimeters. Each part is subdivided transversely into towers and longitudinally into one electromagnetic section (EMC) and either one (in RCAL) or two (in BCAL and FCAL) hadronic sections (HAC). The smallest subdivision of the calorimeter is called a cell. Under test-beam conditions, the CAL single-particle relative energy resolutions were $\sigma(E)/E = 0.18/\sqrt{E}$ for electrons and $\sigma(E)/E = 0.35/\sqrt{E}$ for hadrons, with E in GeV.

The luminosity was measured from the rate of the bremsstrahlung process $ep \rightarrow e\gamma p$. The resulting small-angle energetic photons were measured by the luminosity monitor [12], a lead-scintillator calorimeter placed in the HERA tunnel at $Z = -107$ m.

[1] The ZEUS coordinate system is a right-handed Cartesian system, with the Z axis pointing in the proton beam direction, referred to as the "forward direction", and the X axis pointing left towards the centre of HERA. The coordinate origin is at the nominal interaction point.

4 Data selection and jet search

The data were collected during the running period 1998-2000, when HERA operated with protons of energy $E_p = 920$ GeV and electrons or positrons[2] of energy $E_e = 27.5$ GeV, and correspond to an integrated luminosity of 81.7 ± 1.9 pb^{-1}.

Neutral current DIS events were selected offline using criteria similar to those reported previously [5]. The main steps are listed below.

A reconstructed event vertex consistent with the nominal interaction position was required and cuts based on the tracking information were applied to reduce beam-induced interactions and cosmic-ray events. The scattered-electron candidate was identified using the pattern of energy deposits in the CAL [13]. The energy, E'_e, and polar angle, θ_e, of the electron candidate were also determined from the CAL measurements. The double-angle method [14], which uses θ_e and an angle γ that corresponds, in the quark-parton model, to the direction of the scattered quark, was used to reconstruct Q^2, $Q^2_{\rm DA}$. The angle γ was reconstructed using the CAL measurements of the hadronic final state.

An electron candidate of energy $E'_e > 10$ GeV was required to ensure a high and well understood electron-finding efficiency and to suppress background from photoproduction. The inelasticity variable, y, as reconstructed from the electron, y_e, was required to be below 0.95; this condition removed events in which fake electron candidates from photoproduction background were found in the FCAL. The requirement $38 < (E - p_Z) < 65$ GeV, where E is the total CAL energy and p_Z is the Z component of the energy measured in the CAL cells, to remove events with large initial-state radiation and to reduce further the photoproduction background, was applied. Cosmic rays and beam-related background were rejected by requiring the total missing transverse momentum, $p_T^{\rm miss}$, to be small compared to the total transverse energy, $E_T^{\rm tot}$, $p_T^{\rm miss}/\sqrt{E_T^{\rm tot}} < 3\ \sqrt{\rm GeV}$. The kinematic range was restricted to $Q^2_{\rm DA} > 125$ GeV^2.

The k_T cluster algorithm was used in the longitudinally invariant inclusive mode to reconstruct jets in the hadronic final state from the energy deposits in the CAL cells. The jet algorithm was applied after excluding those cells associated with the scattered-electron candidate. The jets were corrected for detector effects to yield jets of hadrons [5] and events with at least one jet of $E_T^{\rm jet} > 14$ GeV and $-1 < \eta^{\rm jet} < 2.5$ were retained. The final sample comprises those jets that have exactly two subjets for $y_{\rm cut} = 0.05$.

[2] Here and in the following, the term "electron" denotes generically both the electron (e^-) and the positron (e^+), unless otherwise stated.

5 Monte Carlo simulation

Samples of events were generated to determine the response of the detector to jets of hadrons and the correction factors necessary to obtain the hadron-level subjet cross sections. The generated events were passed through the GEANT 3.13-based [15] ZEUS detector- and trigger-simulation programs [9]. They were reconstructed and analysed by the same program chain as the data.

Neutral current DIS events including radiative effects were simulated using the HERACLES 4.6.1 [16] program with the DJANGOH 1.1 [17] interface to the hadronisation programs. HERACLES includes corrections for initial- and final-state radiation, vertex and propagator terms, and two-boson exchange. The QCD cascade is simulated using the colour-dipole model (CDM) [18] including the leading-order (LO) QCD diagrams as implemented in ARIADNE 4.08 [19] and, alternatively, with the MEPS model of LEPTO 6.5 [20]. The CTEQ5D [21] proton PDFs were used for these simulations. Fragmentation into hadrons is performed using the Lund string model [22] as implemented in JETSET [23, 24]

The jet search was performed on the MC events using the energy measured in the CAL cells in the same way as for the data. Using the sample of events generated with either ARIADNE or LEPTO-MEPS and after applying the same offline selection as for the data, a reasonably good description of the measured distributions for the kinematic, jet and subjet variables was found. The average between the acceptance correction values obtained with ARIADNE and LEPTO-MEPS was used to correct the data to the hadron level. The deviations in the results obtained by using either ARIADNE or LEPTO-MEPS to correct the data from their average, were taken to represent systematic uncertainties and range from less than 1% to $\sim$ 10%, depending on the observable. The same jet algorithm was also applied to the hadrons (partons) to obtain the predictions at the hadron (parton) level.

6 Fixed-order calculations

The $\mathcal{O}(\alpha_s)$ and $\mathcal{O}(\alpha_s^2)$ QCD calculations used to compare with the data are based on the program DISENT [25]. The calculations use a generalised version of the subtraction method [26] and are performed in the massless $\overline{\rm MS}$ renormalisation and factorisation schemes. The number of flavours was set to five; the renormalisation (μ_R) and factorisation (μ_F) scales were both set to $\mu_R = \mu_F = Q$; α_s was calculated at two loops using $\Lambda^{(5)}_{\overline{\rm MS}} =$ 220 MeV, which corresponds to $\alpha_s(M_Z) = 0.1175$. The MRST99 [27] parameterisations of the proton PDFs were used.

Since the measurements refer to jets of hadrons, whereas the QCD calculations refer to partons, the predictions were corrected to the hadron level using the MC samples described in Section 5. The multiplicative correction factor, $C_{\rm had}$, defined as the ratio of the subjet cross section for subjets of hadrons over that of partons, was estimated with the MEPS model, since this model reproduces better the shape of the fixed-order QCD calculations. The values of $C_{\rm had}$ were typically in the range $0.8 - 1.2$ for the normalised cross sections and can deviate from unity up to $\pm 50\%$ at the edges of the distributions. Other effects not accounted for in the calculations, namely QED radiative corrections and Z^0 exchange, were found to be very small for the normalised cross-section calculations and, therefore, neglected.

The following theoretical uncertainties were considered:

- the uncertainty on the fixed-order calculations due to higher-order terms, which was estimated by varying μ_R between $Q/2$ and $2Q$;
- the uncertainty due to the hadronisation corrections, which was estimated as the difference between the $C_{\rm had}$ factors computed using the CDM and MEPS models. This uncertainty is dominant.

These uncertainties were added in quadrature and are shown as hatched bands in Figs. 5 to 8.

7 Systematic uncertainties

The following sources of systematic uncertainty were considered for the measured subjet cross sections:

- the uncertainty in the absolute energy scale of the jets was estimated to be $\pm 1\%$ [1,28];
- the uncertainty in the absolute energy scale of the electron candidate was estimated to be $\pm 1\%$ [29];
- the deviations in the results obtained by using either Ariadne or Lepto-MEPS to correct the data from their average, were taken to represent systematic uncertainties;
- the uncertainty in the simulation of the trigger.

The effect of these uncertainties on the normalised cross sections is small compared to the statistical uncertainties for the measurements presented in Section 8. The systematic uncertainties were added in quadrature to the statistical uncertainties and are shown as error bars in the figures.

8 Results

Using the selected data sample, normalised differential subjet cross sections were measured for $Q^2 > 125$ GeV^2. The cross sections were determined for those jets with $E_T^{\rm jet} > 14$ GeV and $-1 < \eta^{\rm jet} < 2.5$ which have two subjets for $y_{\rm cut} = 0.05$.

The cross-section $(1/\sigma)(d\sigma/d(E_T^{\rm sbj}/E_T^{\rm jet}))$ is presented in Fig. 1a. The distribution of the fraction of transverse energy contains two entries per jet and is symmetric with respect to $E_T^{\rm sbj}/E_T^{\rm jet} = 0.5$ by construction. The data distribution has a peak at $E_T^{\rm sbj}/E_T^{\rm jet} = 0.5$, which shows that the two subjets tend to have similar transverse energies. The distribution of $\eta^{\rm sbj} - \eta^{\rm jet}$ is shown in Fig. 1b and also has two entries per jet. The measured cross section has a two-peak structure; the dip at $\eta^{\rm sbj} - \eta^{\rm jet} \sim 0$ comes from the fact that the subjets cannot be reconstructed too close together. Figure 1c presents the normalised cross section as a function of $|\phi^{\rm sbj} - \phi^{\rm jet}|$. There are two entries per jet in this distribution. The data distribution has a peak at $|\phi^{\rm sbj} - \phi^{\rm jet}| = 0.2 - 0.3$; the suppression at $|\phi^{\rm sbj} - \phi^{\rm jet}| \sim 0$ comes also from the fact that the subjets cannot be resolved when they are too close together. The distribution as a function of $\alpha^{\rm sbj}$ (one entry per jet) increases as $\alpha^{\rm sbj}$ increases (see Fig. 1d). This shows that the highest transverse energy subjet tends to be in the rear direction. This is consistent with the asymmetric peaks observed in the $\eta^{\rm sbj} - \eta^{\rm jet}$ distribution. Figures 2 to 4 show the normalised cross sections in different regions of $E_T^{\rm jet}$. Even though the mean subjet multiplicity decreases with increasing $E_T^{\rm jet}$ [4], the measured normalised differential subjet cross sections have very similar shapes in all $E_T^{\rm jet}$ regions for each observable. This means that the subjet topology does not change significantly with $E_T^{\rm jet}$.

Leading-logarithm parton-shower Monte Carlo calculations using either MEPS or CDM are compared to the data in Figs. 1 to 4. The prediction of CDM gives a good description of the data distribution of $E_T^{\rm sbj}/E_T^{\rm jet}$, whereas that of MEPS gives a somewhat poorer description. Both models give a reasonable description of the data distribution of $\eta^{\rm sbj} - \eta^{\rm jet}$ in the region $|\eta^{\rm sbj} - \eta^{\rm jet}| < 0.5$. MEPS describes the data distribution of $|\phi^{\rm sbj} - \phi^{\rm jet}|$ well, whereas CDM gives a poorer description. Both models give a reasonable description of the data for $\alpha^{\rm sbj}$. For the $E_T^{\rm jet}$ dependence of the normalised cross sections, MEPS and CDM give a reasonable description of the measured dependence.

Fixed-order QCD calculations are compared to the data in Figs. 5 to 8. The QCD predictions give a good description of the data in shape. In particular, the calculation of the cross section as a function of $E_T^{\rm sbj}/E_T^{\rm jet}$ exhibits a peak at $E_T^{\rm sbj}/E_T^{\rm jet} = 0.5$, as seen in the data. The calculations for the $\eta^{\rm sbj} - \eta^{\rm jet}$ and $\alpha^{\rm sbj}$ distributions predict that the highest transverse energy subjet tends to be in the rear direction, in agreement with the data. This shows that the mechanism driving the subjet topology are the $q \to qg$ and $g \to q\bar{q}$ subprocesses as implemented in the pQCD calculations.

To gain further insight into the pattern of parton radiation, the predictions for quark- and gluon-induced processes are compared separately with the data in Fig. 9. The NLO calculations predict that the two-subjet rate is dominated by quark-induced processes: the relative contribution of quark- (gluon-) induced processes is 82% (18%). The predictions for these two types of processes are different: in quark-induced processes, the two subjets have more similar transverse energies (see Fig. 9a) and are closer to each other (see Fig. 9b and 9c) than in gluon-induced processes. The comparison with the measurements shows that the data are better described by the calculations for jets arising from a qg pair than those coming from a $q\bar{q}$ pair.

9 Summary

Measurements of normalised differential subjet cross sections in inclusive-jet NC DIS production have been made in ep collisions using 81.7 pb^{-1} of data collected with the ZEUS detector at HERA. The cross sections refer to jets identified in the laboratory frame with the k_T cluster algorithm in the longitudinally invariant inclusive mode and selected with $E_T^{\rm jet} > 14$ GeV and $-1 < \eta^{\rm jet} < 2.5$. The measurements were made for those jets which have two subjets for $y_{\rm cut} = 0.05$ in the kinematic region defined by $Q^2 > 125$ GeV^2.

Normalised differential subjet cross sections were measured as functions of $E_T^{\rm sbj}/E_T^{\rm jet}$, $\eta^{\rm sbj} - \eta^{\rm jet}$, $|\phi^{\rm sbj} - \phi^{\rm jet}|$ and $\alpha^{\rm sbj}$. The data shows that the two subjets tend to have similar transverse energies and that the highest transverse energy subjet tends to be in the rear direction. A reasonable description of the data is obtained by fixed-order QCD calculations. This means that the pattern of parton radiation as predicted by QCD reproduces the subjet topology in the data. Furthermore, the subjet distributions in the data are well described by the calculations for jets arising from a quark-gluon pair.

Acknowledgements

We thank the DESY Directorate for their strong support and encouragement. The remarkable achievements of the HERA machine group were essential for the successful completion of this work and are greatly appreciated.

References

[1] ZEUS Coll., S. Chekanov et al., Phys. Lett. **B 531**, 9 (2002);
ZEUS Coll., S. Chekanov et al., Eur. Phys. J. **C 23**, 615 (2002).

[2] ZEUS Coll., J. Breitweg et al., Phys. Lett. **B 507**, 70 (2001);
ZEUS Coll., S. Chekanov et al., Phys. Lett. **B 547**, 164 (2002);
ZEUS Coll., S. Chekanov et al., Phys. Lett. **B 560**, 7 (2003);
ZEUS Coll., J. Chekanov et al., Eur. Phys. J. **C 31**, 149 (2003);
ZEUS Coll., S. Chekanov et al., Eur. Phys. J. **C 23**, 13 (2002);
ZEUS Coll., J. Breitweg et al., Phys. Lett. **B 443**, 394 (1998).

[3] H1 Coll., C. Adloff et al., Eur. Phys. J. **C 19**, 289 (2001);
H1 Coll., C. Adloff et al., Eur. Phys. J. **C 25**, 13 (2002);
H1 Coll., C. Adloff et al., Phys. Lett. **B 542**, 193 (2002);
H1 Coll., C. Adloff et al., Eur. Phys. J. **C 29**, 497 (2003);
H1 Coll., C. Adloff et al., Eur. Phys. J. **C 19**, 429 (2001);
H1 Coll., C. Adloff et al., Phys. Lett. **B 515**, 17 (2001).

[4] ZEUS Coll., S. Chekanov et al., Phys. Lett. **B 558**, 41 (2003).

[5] ZEUS Coll., S. Chekanov et al., Nucl. Phys. **B 700**, 3 (2004).

[6] S. Catani et al., Nucl. Phys. **B 406**, 187 (1993).

[7] S.D. Ellis and D.E. Soper, Phys. Rev. **D 48**, 3160 (1993).

[8] ZEUS Coll., M. Derrick et al., Phys. Lett. **B 293**, 465 (1992).

[9] ZEUS Coll., U. Holm (ed.), *The ZEUS Detector*. Status Report (unpublished), DESY (1993), available on `http://www-zeus.desy.de/bluebook/bluebook.html`.

[10] N. Harnew et al., Nucl. Inst. Meth. **A 279**, 290 (1989);
B. Foster et al., Nucl. Phys. Proc. Suppl. **B 32**, 181 (1993);
B. Foster et al., Nucl. Inst. Meth. **A 338**, 254 (1994).

[11] M. Derrick et al., Nucl. Inst. Meth. **A 309**, 77 (1991);
A. Andresen et al., Nucl. Inst. Meth. **A 309**, 101 (1991);
A. Caldwell et al., Nucl. Inst. Meth. **A 321**, 356 (1992);
A. Bernstein et al., Nucl. Inst. Meth. **A 336**, 23 (1993).

[12] J. Andruszków et al., Preprint DESY-92-066, DESY, 1992;
ZEUS Coll., M. Derrick et al., Z. Phys. **C 63**, 391 (1994);
J. Andruszków et al., Acta Phys. Pol. **B 32**, 2025 (2001).

[13] H. Abramowicz, A. Caldwell and R. Sinkus, Nucl. Inst. Meth. **A 365**, 508 (1995);
R. Sinkus and T. Voss, Nucl. Inst. Meth. **A 391**, 360 (1997).

[14] S. Bentvelsen, J. Engelen and P. Kooijman, *Proc. of the Workshop on Physics at HERA*, W. Buchmüller and G. Ingelman (eds.), Vol. 1, p. 23. Hamburg, Germany, DESY (1992);
K.C. Höger, ibid., p. 43.

[15] R. Brun et al., GEANT3, Technical Report CERN-DD/EE/84-1, CERN, 1987.

[16] A. Kwiatkowski, H. Spiesberger and H.-J. Möhring, Comp. Phys. Comm. **69**, 155 (1992);
H. Spiesberger, *An Event Generator for ep Interactions at HERA Including Radiative Processes (Version 4.6)*, 1996, available on
`http://www.desy.de/~hspiesb/heracles.html`.

[17] K. Charcuła, G.A. Schuler and H. Spiesberger, Comp. Phys. Comm. **81**, 381 (1994);
H. Spiesberger, HERACLES *and* DJANGOH*: Event Generation for ep Interactions at HERA Including Radiative Processes*, 1998, available on
`http://www.desy.de/~hspiesb/djangoh.html`.

[18] Y. Azimov et al., Phys. Lett. **B 165**, 147 (1985);
G. Gustafson, Phys. Lett. **B 175**, 453 (1986);
G. Gustafson and U. Pettersson, Nucl. Phys. **B 306**, 746 (1988);
B. Andersson et al., Z. Phys. **C 43**, 625 (1989).

[19] L. Lönnblad, Comp. Phys. Comm. **71**, 15 (1992);
L. Lönnblad, Z. Phys. **C 65**, 285 (1995).

[20] G. Ingelman, A. Edin and J. Rathsman, Comp. Phys. Comm. **101**, 108 (1997).

[21] H.L. Lai et al., Eur. Phys. J. **C 12**, 375 (2000).

[22] B. Andersson et al., Phys. Rep. **97**, 31 (1983).

[23] T. Sjöstrand, Comp. Phys. Comm. **82**, 74 (1994);
T. Sjöstrand et al., Comp. Phys. Comm. **135**, 238 (2001).

[24] T. Sjöstrand, Comp. Phys. Comm. **39**, 347 (1986);
T. Sjöstrand and M. Bengtsson, Comp. Phys. Comm. **43**, 367 (1987).

[25] S. Catani and M.H. Seymour, Nucl. Phys. **B 485**, 291 (1997). Erratum in Nucl. Phys. **B 510**, 503 (1998).

[26] R.K. Ellis, D.A. Ross and A.E. Terrano, Nucl. Phys. **B 178**, 421 (1981).

[27] A.D. Martin et al., Eur. Phys. J. **C 4**, 463 (1998);
A.D. Martin et al., Eur. Phys. J. **C 14**, 133 (2000).

[28] M. Wing (on behalf of the ZEUS Coll.), *Proc. of the 10th International Conference on Calorimetry in High Energy Physics*, R. Zhu (ed.), p. 767. Pasadena, USA (2002). Also in preprint hep-ex/0206036.

[29] ZEUS Coll., S. Chekanov et al., Eur. Phys. J. **C 21**, 443 (2001).

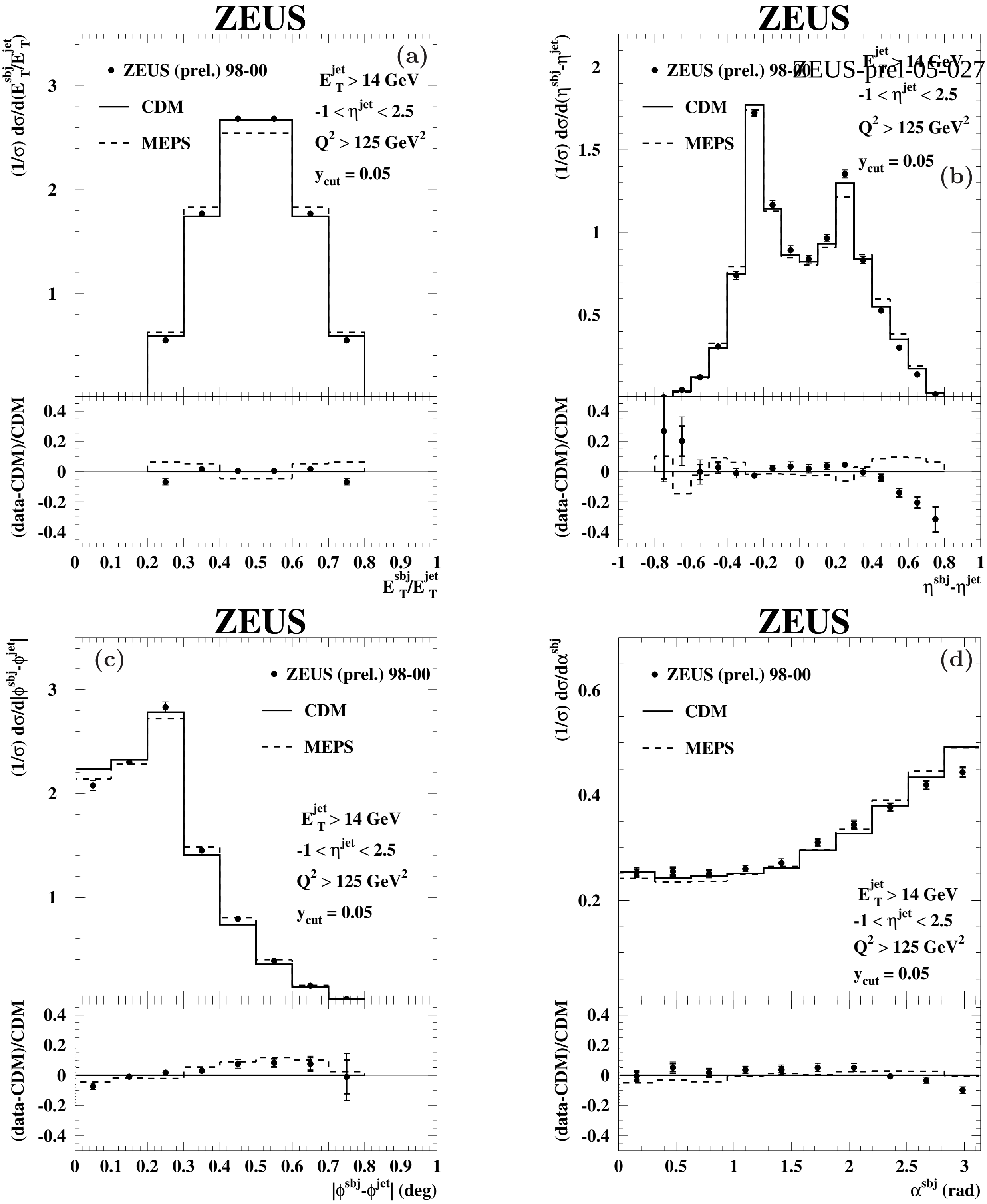

Figure 1: *Measured normalised differential subjet cross sections for jets with $E_T^{\rm jet} > 14$ GeV and $-1 < \eta^{\rm jet} < 2.5$ which have two subjets for $y_{\rm cut} = 0.05$ as functions of (a) $E_T^{\rm sbj}/E_T^{\rm jet}$, (b) $\eta^{\rm sbj} - \eta^{\rm jet}$, (c) $|\phi^{\rm sbj} - \phi^{\rm jet}|$ and (d) $\alpha^{\rm sbj}$ (dots). The thick error bars represent the statistical uncertainties of the data, and the thin error bars show the statistical and systematic uncertainties added in quadrature. For comparison, the predictions of the leading-logarithm parton-shower Monte Carlo models of CDM (solid histograms) and MEPS (dashed histograms) are included. The lower part of the figures displays the fractional difference between the measured normalised cross section and the corresponding predictions of CDM (dots); the fractional difference between the predictions of MEPS and CDM is also shown (dashed histograms).*

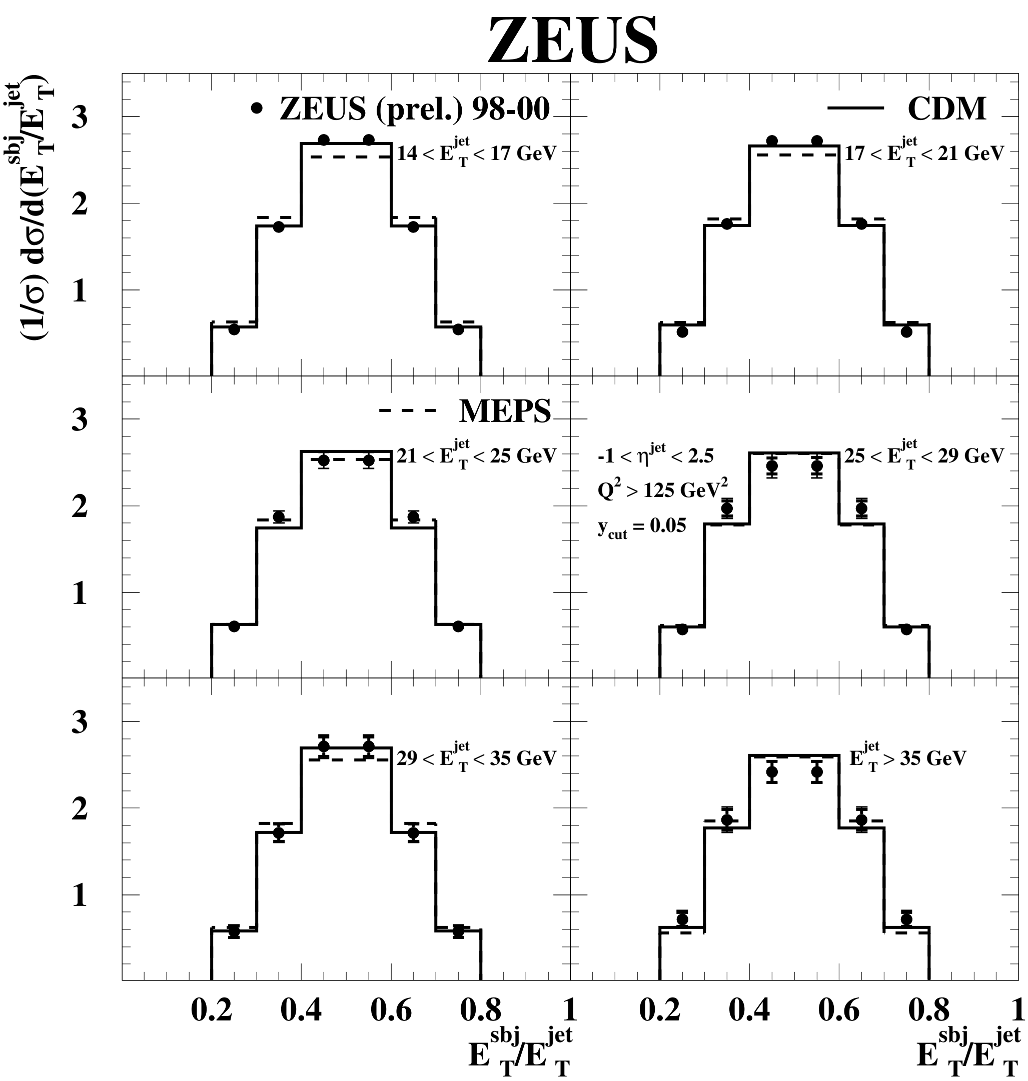

Figure 2: *Measured normalised differential subjet cross sections for jets with* $-1 < \eta^{\rm jet} < 2.5$ *which have two subjets for* $y_{\rm cut} = 0.05$ *as a function of* $E_T^{\rm sbj}/E_T^{\rm jet}$ *in different regions of* $E_T^{\rm jet}$ *(dots). Other details are as in the caption to Fig. 1.*

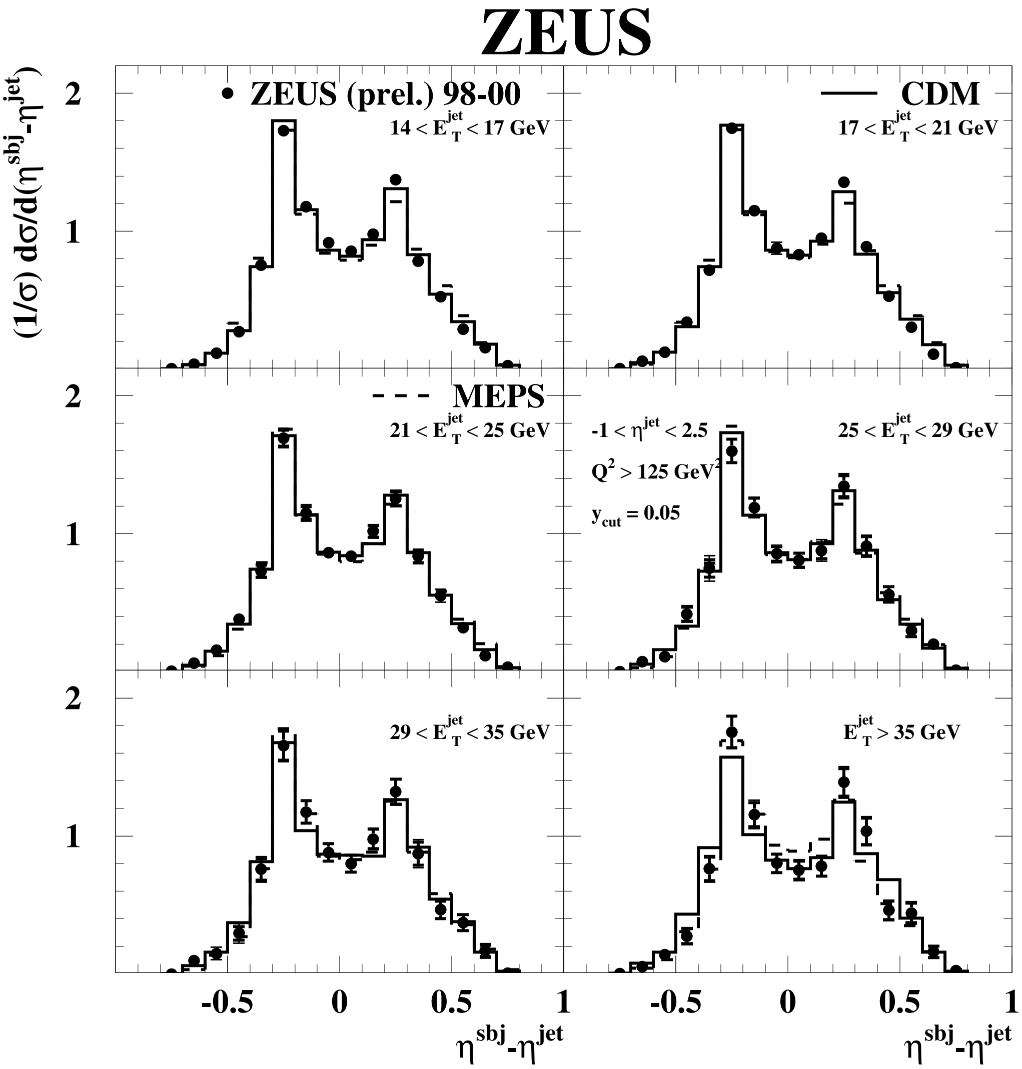

Figure 3: *Measured normalised differential subjet cross sections for jets with* $-1 < \eta^{\rm jet} < 2.5$ *which have two subjets for* $y_{\rm cut} = 0.05$ *as a function of* $\eta^{\rm sbj} - \eta^{\rm jet}$ *in different regions of* $E_T^{\rm jet}$ *(dots). Other details are as in the caption to Fig. 1.*

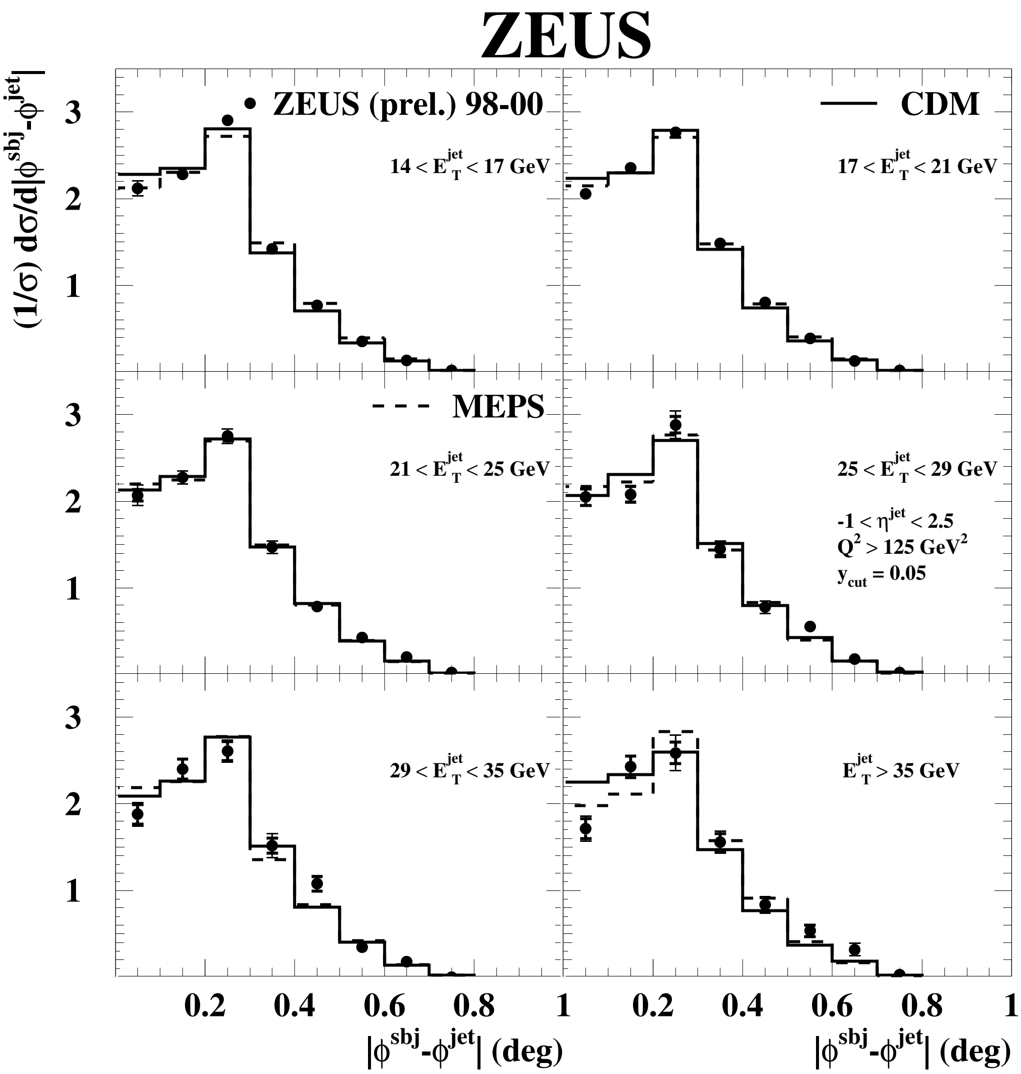

Figure 4: *Measured normalised differential subjet cross sections for jets with $-1 < \eta^{\rm jet} < 2.5$ which have two subjets for $y_{\rm cut} = 0.05$ as a function of $|\phi^{\rm sbj} - \phi^{\rm jet}|$ in different regions of $E_T^{\rm jet}$ (dots). Other details are as in the caption to Fig. 1.*

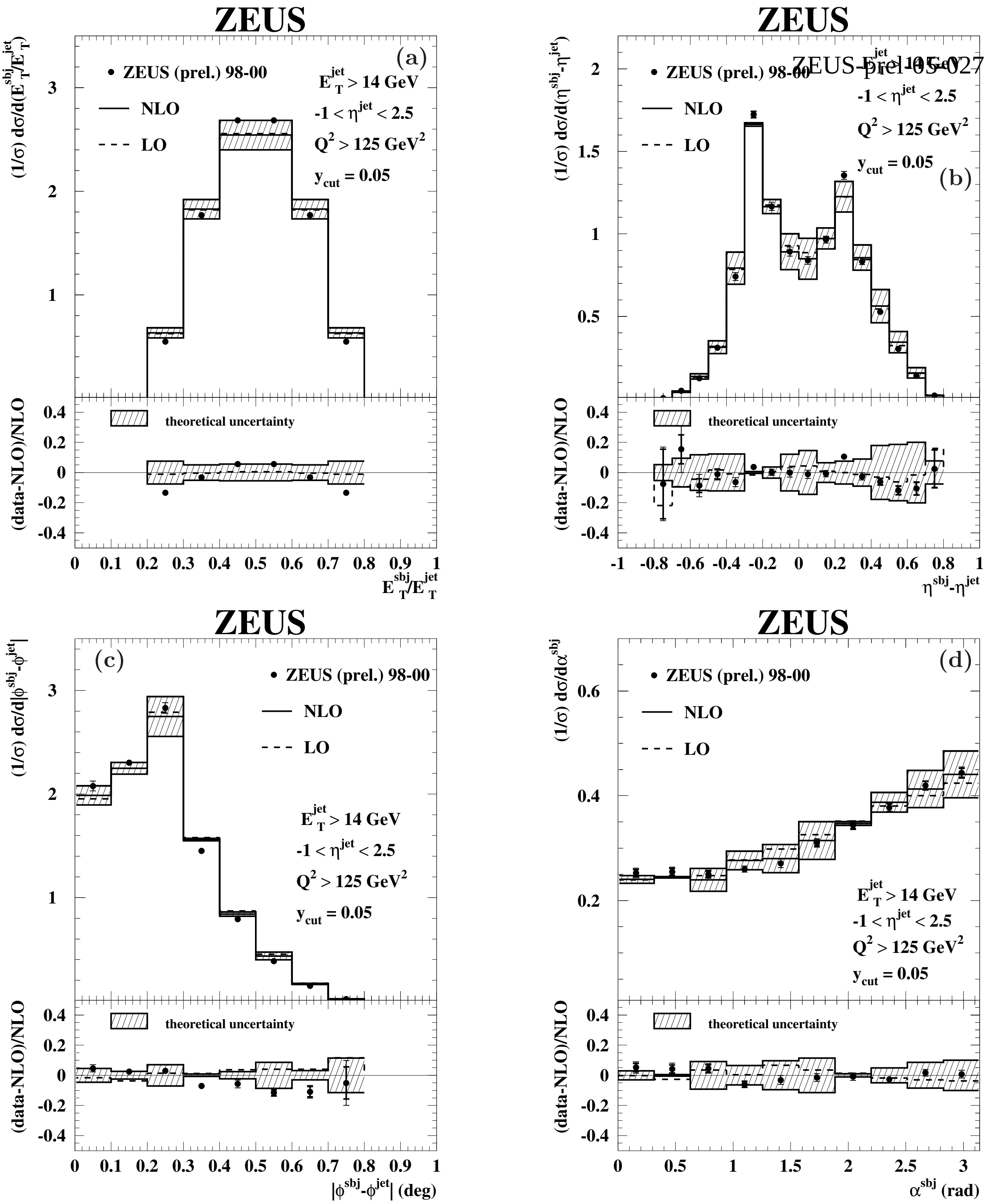

Figure 5: *Measured normalised differential subjet cross sections for jets with $E_T^{\rm jet} > 14$ GeV and $-1 < \eta^{\rm jet} < 2.5$ which have two subjets for $y_{\rm cut} = 0.05$ as functions of (a) $E_T^{\rm sbj}/E_T^{\rm jet}$, (b) $\eta^{\rm sbj} - \eta^{\rm jet}$, (c) $|\phi^{\rm sbj} - \phi^{\rm jet}|$ and (d) $\alpha^{\rm sbj}$ (dots). For comparison, the predictions of* DISENT *at LO (dashed histograms) and NLO (solid histograms) are included. The hatched bands represent the theoretical uncertainty of the NLO prediction. The lower part of the figures displays the fractional difference between the measured normalised cross section and the corresponding predictions at NLO (dots); the fractional difference between the LO and NLO predictions is also shown (dashed histograms). Other details are as in the caption to Fig. 1.*

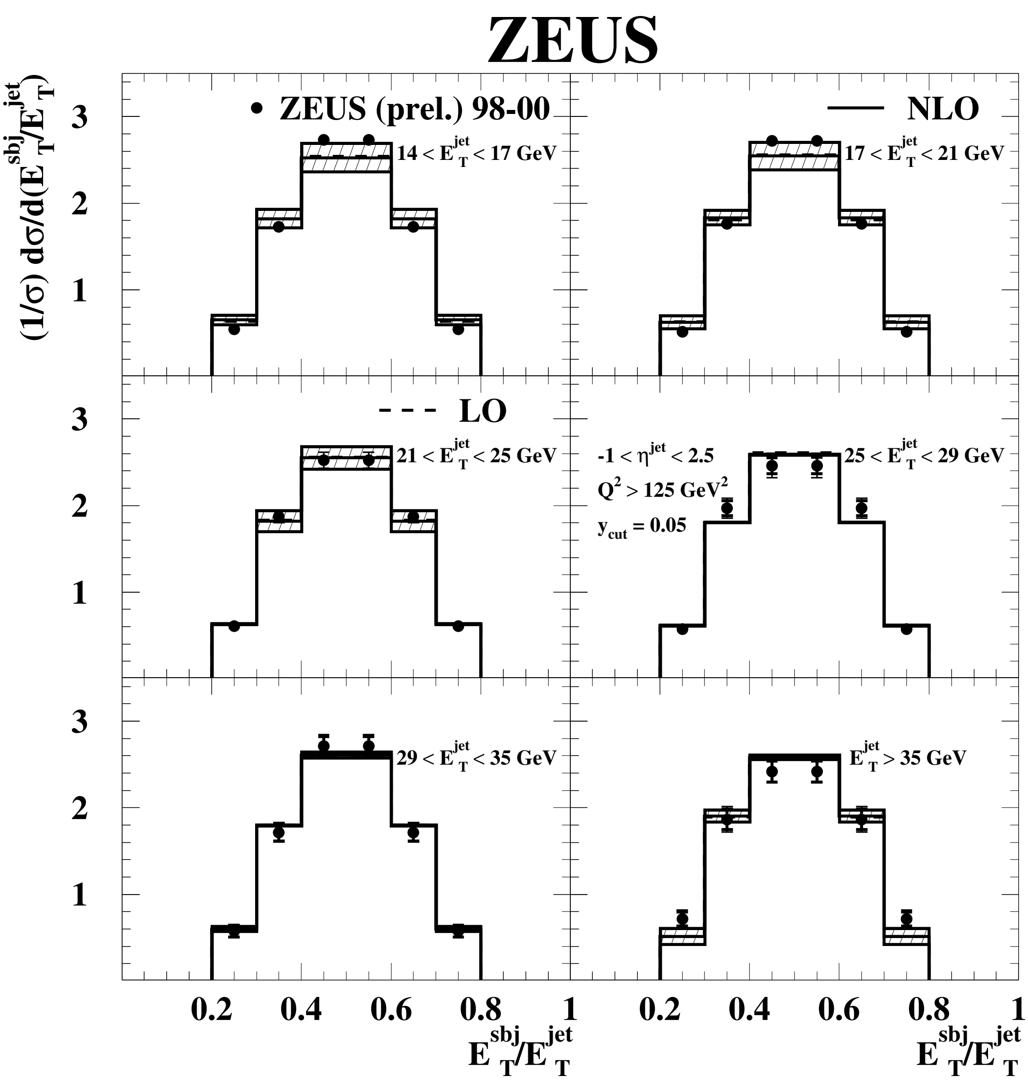

Figure 6: *Measured normalised differential subjet cross sections for jets with* $-1 < \eta^{\rm jet} < 2.5$ *which have two subjets for* $y_{\rm cut} = 0.05$ *as a function of* $E_T^{\rm sbj}/E_T^{\rm jet}$ *in different regions of* $E_T^{\rm jet}$ *(dots). Other details are as in the caption to Fig. 5.*

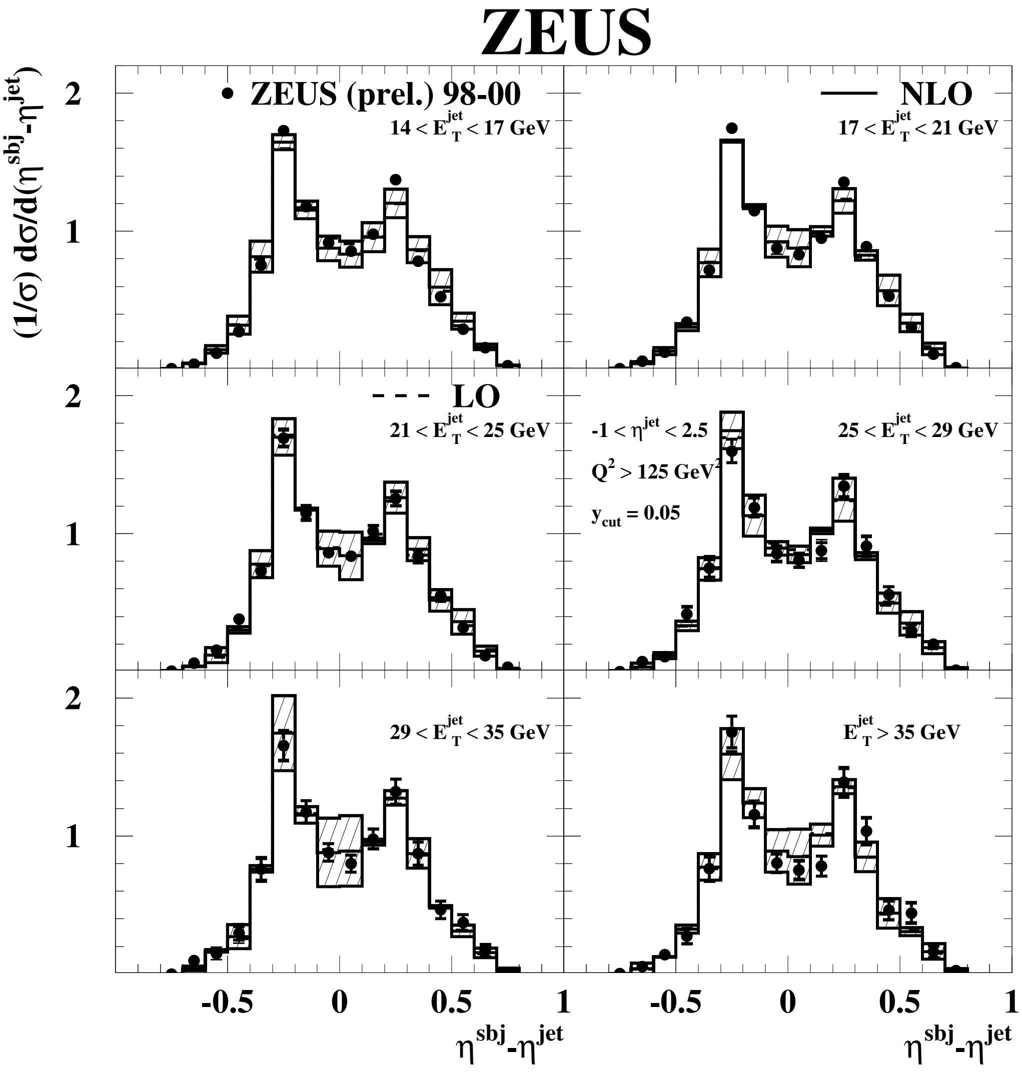

Figure 7: *Measured normalised differential subjet cross sections for jets with* $-1 < \eta^{\rm jet} < 2.5$ *which have two subjets for* $y_{\rm cut} = 0.05$ *as a function of* $\eta^{\rm sbj} - \eta^{\rm jet}$ *in different regions of* $E_T^{\rm jet}$ *(dots). Other details are as in the caption to Fig. 5.*

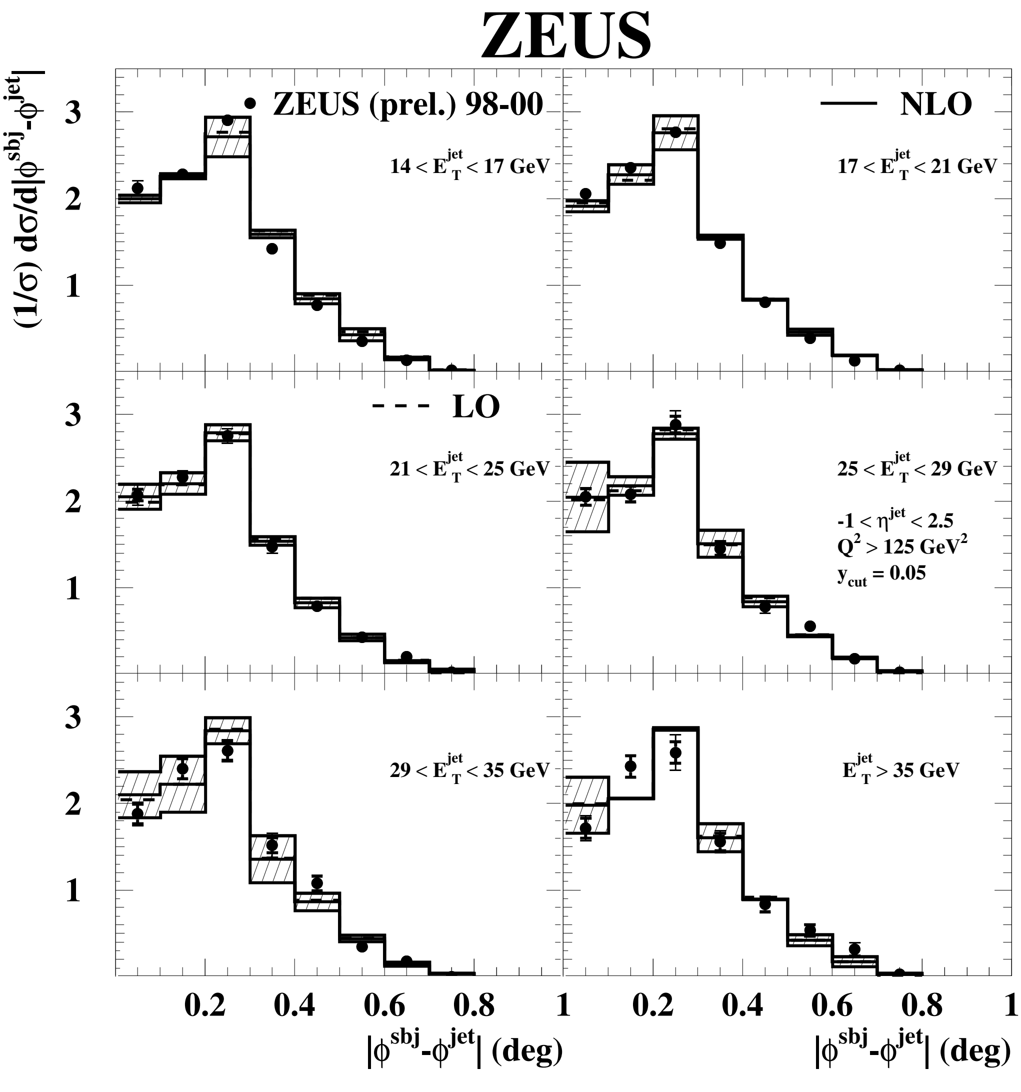

Figure 8: *Measured normalised differential subjet cross sections for jets with* $-1 < \eta^{\rm jet} < 2.5$ *which have two subjets for* $y_{\rm cut} = 0.05$ *as a function of* $|\phi^{\rm sbj} - \phi^{\rm jet}|$ *in different regions of* $E_T^{\rm jet}$ *(dots). Other details are as in the caption to Fig. 5.*

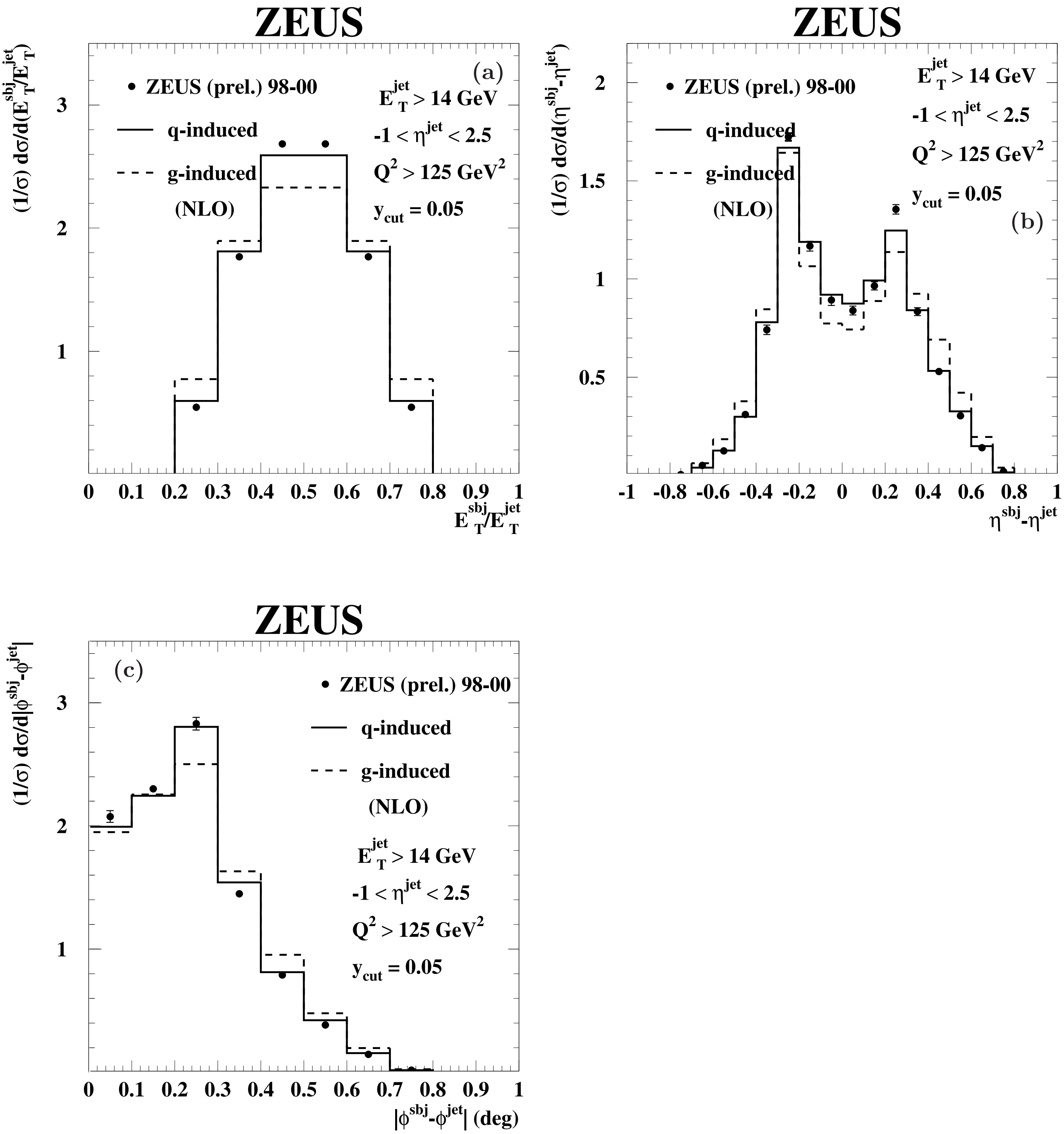

Figure 9: *Measured normalised differential subjet cross sections for jets with $E_T^{\mathrm{jet}} > 14$ GeV and $-1 < \eta^{\mathrm{jet}} < 2.5$ which have two subjets for $y_{\mathrm{cut}} = 0.05$ as functions of (a) $E_T^{\mathrm{sbj}}/E_T^{\mathrm{jet}}$, (b) $\eta^{\mathrm{sbj}} - \eta^{\mathrm{jet}}$ and (c) $|\phi^{\mathrm{sbj}} - \phi^{\mathrm{jet}}|$. For comparison, the NLO predictions for quark- (solid histograms) and gluon-induced (dashed histograms) processes are included. Other details are as in the caption to Fig. 1.*